Non-uniqueness of transonic flow in an intake-type channel

Non-uniqueness of transonic flow in an intake-type channel

A. Kuzmin

St. Petersburg State University, 28 University Ave., St. Petersburg 198504, Russia

E-mail: a.kuzmin@spbu.ru

Abstract. The two-dimensional turbulent airflow in a 9-degrees-bent channel is studied numerically. Inner surfaces of the top and bottom walls are parallel to each other upstream and downstream of the bend. The free stream is supersonic, whereas the flow is subsonic at the channel exit. Solutions of the Reynolds-averaged Navier-Stokes equations are obtained with a finite-volume solver using the Spalart-Allmaras and Shear Stress Transport $k-\omega$ turbulence models. The solutions reveal a flow hysteresis and non-uniqueness in considerable bands of the free-stream Mach number, angle of attack, and exit pressure. At the endpoints of the bands, there are abrupt changes of the shock wave system. The non-uniqueness admits different losses of the total pressure, which may cause different trusts of an air breathing engine.

1. Introduction

Both inviscid and turbulent supersonic airflows in convergent channels involve shock waves which are known to be unstable. The instability can be explained using quasi-one-dimensional equations which govern mass flow rate and stagnation temperature across the normal shock [1]. Recently, instability of shocks was also revealed in bent channels whose cross section is either constant or slightly increasing [2, 3]. In the latter case, the instability is caused by an interaction of a shock wave formed in front of the concave wall with an expansion flow developed over the opposite (convex) wall. The interaction causes a hysteresis phenomenon under gradual variations of the outlet pressure, free-stream Mach number M_∞ or angle of attack α.

In practice, transonic flow in curved/bent channels occurs, e.g., in Y-shaped intakes of battle-plane and fighter aircraft engines. Kotteda and Mittal [4] studied the effect of sideslip angle on the performance of a slightly divergent Y-intake and identified non-unique flow regimes as a result of these variations; also an effect of the initial condition was investigated. Feng *et al.* [5] performed a numerical and experimental study of supersonic flow in a bent channel modeling a variable geometry dual mode combustor. The study indicated that the pressure distribution on the wall had an obvious hysteresis under continuous variations of the outlet cross section area.

In [6] we considered an intake-type channel with a short top wall and parallel inner surfaces of walls before and after the bend section. A dependence of 2D shock positions on M_∞ at zero and negative angles of attack was studied, and considerable attention was paid to a subsonic exit condition in contrast to the supersonic condition used in a previous paper [7].

In the present paper, we examine a channel with a displacement of the bottom wall bend downstream with respect to the top wall bend. This results in a smaller exit section of the channel and larger Mach numbers that produce the instability of shocks. In Sections 2 and 3

we formulate the problem and outline a numerical method. Section 4 addresses locations of a shock wave versus M_∞ at a given angle of attack; the flow non-uniqueness and losses of the total pressure are discussed. In Section 5 we study the shock position as a function of the angle of attack at a given M_∞. Effects of the exit pressure and a replacement of the bottom bend by a local circular arc are analyzed in Section 6.

2. Problem formulation

We consider a channel whose top wall is a compression corner

$$y = 30 \quad \text{at} \quad -28 \le x \le 0, \qquad y = 30 - x\,\tan 9^\circ \quad \text{at} \quad 0 \le x \le 50,$$

whereas the bottom wall is an expansion corner

$$y = 0 \quad \text{at} \quad -68 \le x \le 8, \qquad y = (8 - x)\,\tan 9^\circ \quad \text{at} \quad 8 \le x \le 50, \tag{1}$$

see Fig. 1. Here and further in the paper, the Cartesian coordinates (x, y) are dimensional and given in millimeters. The outer surfaces of the top and bottom walls are a corner and segment, respectively. The thickness of leading edges of the walls is 0.05.

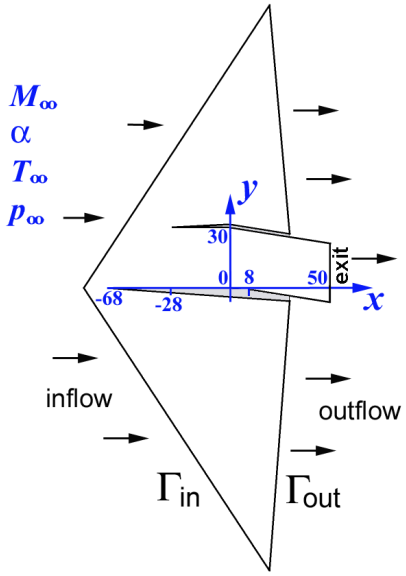

Figure 1. Sketch of the channel and computational domain.

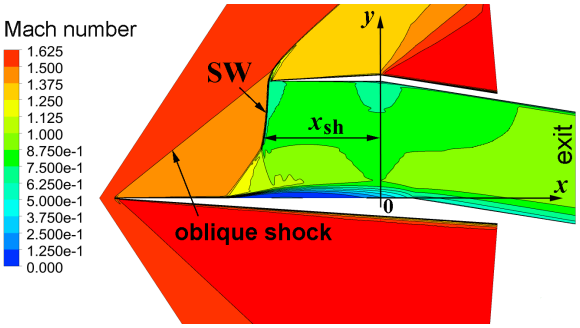

Figure 2. Mach number contours and expelled shock wave SW at $\alpha = -5^\circ$, $M_\infty = 1.62$, $p_{\text{exit}} = 2 \times 10^5$ N/m^2.

The inflow boundary Γ_{in} of the computational domain is formed by two segments with the beginnings at the point $y = 0$, $x = -72$ and ends at $x = 20$, $y = \pm 140$. We prescribe the $x-$ and $y-$components of the velocity on Γ_{in} as follows: $U_\infty = M_\infty a_\infty \cos\alpha$, $V_\infty = M_\infty a_\infty \sin\alpha$, where $M_\infty > 1$. In addition, we impose on Γ_{in} the static pressure p_∞, the turbulence level of 1%, and static temperature $T_\infty = 200$ K which determines the sound speed $a_\infty = 283.58$ m/s.

The outflow boundary Γ_{out} of the computational domain is constituted by two segments with the beginnings on the outer surfaces of walls at $x = 30$ and ends at $x = 20$, $y = \pm 140$. We prescribe the condition $M > 1$ on Γ_{out}. At the channel exit $x = 50$ we impose the subsonic condition $M_{\text{exit}} < 1$ along with the static pressure p_{exit}. The vanishing heat flux and no-slip condition are imposed on the walls. The air is treated as a perfect gas, whose specific heat at constant pressure is 1004.4 J/(kg K) and the ratio of specific heats is 1.4. We use the Sutherland formula for the molecular dynamic viscosity and adopt the value of 28.96 kg/kmol for the molar mass. The pressure p_∞ is set to 8×10^4 N/m^2 throughout the paper, except for Fig. 9 in which

we compare results obtained for this and tripled free-stream pressure. The Reynolds number based on $p_\infty = 8 \times 10^4$ N/m^2, $M_\infty = 1.6$, and height of the channel is 1.4×10^6. Initial data are either parameters of the free stream or a flow field calculated for other α, M_∞ or p_{exit}.

3. Numerical method

Solutions of the unsteady Reynolds-averaged Navier-Stokes equations were obtained with an ANSYS-18.2 CFX finite-volume solver of second-order accuracy. An implicit backward Euler scheme was employed for the time-accurate computations. We used the Shear Stress Transport $k-\omega$ and Spalart-Allmaras turbulence models, which are known to reasonably predict aerodynamic flows with boundary layer separations [8, 9].

Computations were performed on hybrid unstructured meshes constituted by quadrangles in 38 layers on the walls and by triangles in the remaining region. The non-dimensional thickness y^+ of the first mesh layer on the walls was less than 1. The sizes of triangles essentially decreased in the channel to resolve shock waves accurately. Test solutions obtained on uniformly refined meshes of approximately 2×10^5, 4×10^5, and 8×10^5 cells showed that a discrepancy between shock wave coordinates obtained on the second and third meshes did not exceed 1%. Global time steps of 5×10^{-7} s and 10^{-6} s yielded indistinguishable solutions. For this reason, the time step of 10^{-6} s and mesh of 4×10^5 cells were employed for the study of 2D flow hysteresis at various α, M_∞, and p_{exit}. The root-mean-square CFL number (over mesh cells) was about 2.

For the solver validation, we recomputed several benchmark transonic flow problems and obtained good agreement with results available in the literature, see [6, 7]. Computations were run on Huawei RH2288H computational nodes using a splitting of a task among 96 cores.

4. Shock wave location as a function of M_∞ at $\alpha = -5°$.

First, we solved the problem at $M_\infty = 1.55$, $\alpha = -5°$ using the free-stream parameters for initialization of the solution. Computations showed a convergence of time-dependent mean parameters of turbulent flow to a steady state in less than 0.1 s of physical time. The obtained flow field exhibits an oblique shock attached to the leading edge of bottom wall, and a shock SW located closer to the entrance ($x_{\text{entrance}} = -28$, $0 < y < 30$). When M_∞ increases step-by-step from 1.55 to 1.62, the shock SW shifts downstream and becomes nearly normal, see Fig. 2; at each step for initial conditions we used the flow field obtained at the previous M_∞. Such a flow pattern is called hereafter the flow regime with an expelled SW.

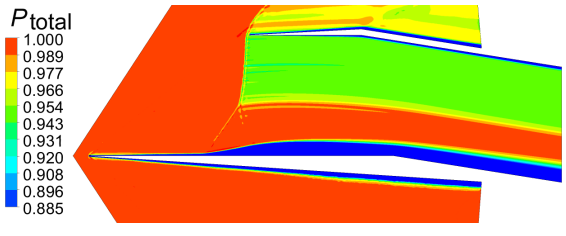

Figure 3. Contours of the non-dimensional total pressure P_{total} in the flow depicted in Fig. 2.

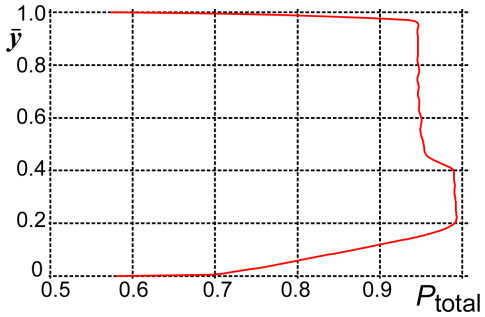

Figure 4. P_{total} in the exit section of the flow depicted in Fig. 2 versus the non-dimensional distance $\bar{y}$ from the bottom wall; $\bar{y} = 1$ corresponds to the top wall.

Figures 3 and 4 illustrate distributions of the non-dimensional total pressure $P_{\text{total}} = p_{\text{total}}/p_{\text{total},\infty}$ in the flow displayed in Fig. 2, where $p_{\text{total},\infty} = 350,280$ N/m^2 is the stagnation pressure.

To analyze streamwise positions of SW, we will trace its coordinate $x_{\rm sh}$ at the height $y = 15$. The lower branch of solid curve 1 in Fig. 5 shows that $x_{\rm sh}$ gradually increases when M_∞ increases from 1.55 to 1.625. Further increase of M_∞ triggers the swallowing of SW and transition from the lower branch of curve 1 to the upper one. After that a slight decrease of M_∞ to 1.62 yields a flow with the swallowed SW, see Fig. 6, which essentially differs from that displayed in Fig. 2 for the same M_∞.

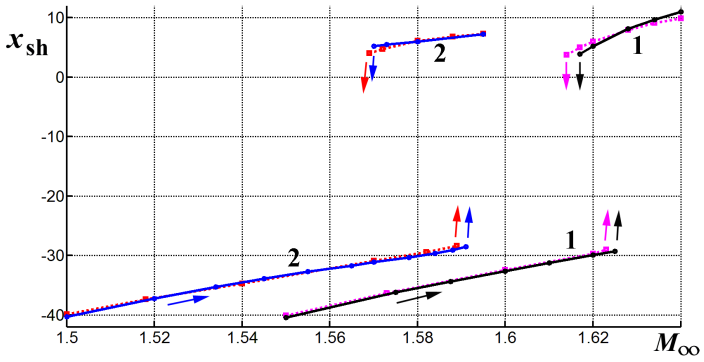

Figure 5. Coordinate $x_{\rm sh}$ of the shock wave SW versus M_∞ at $\alpha = -5°$: curve 1 – $p_{\rm exit} = 2 \times 10^5$ N/m^2, curve 2 – $p_{\rm exit} = 1.8 \times 10^5$ N/m^2. Solid curves – SST $k-\omega$ turbulence model [8]; dashed curves – Spalart-Allmaras turbulence model [9]. The upper (lower) branches of the curves correspond to flow regimes with the swallowed (expelled) SW.

Further decrease of M_∞ from 1.62 to values smaller than 1.616 triggers an expulsion of SW from the channel. This means a transition to the lower branch of curve 1 in Fig. 5. Due to the hysteresis, the flow is non-unique in the band $1.617 \le M_\infty \le 1.625$.

Computations using the Spalart-Allmaras turbulence model instead of SST $k-\omega$ produced results which are very close to those discussed above (cf. dashed and solid curves in Fig. 5).

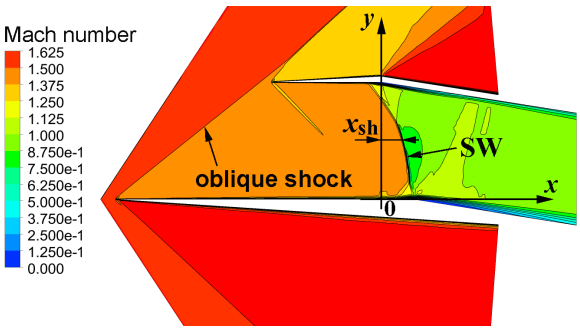

Figure 6. Mach number contours and swallowed shock wave SW at $\alpha = -5°$, $M_\infty = 1.62$, $p_{\rm exit} = 2 \times 10^5$ N/m^2.

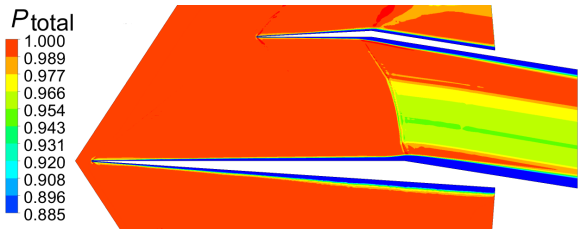

Figure 7. Contours of the non-dimensional total pressure in the flow depicted in Fig. 6.

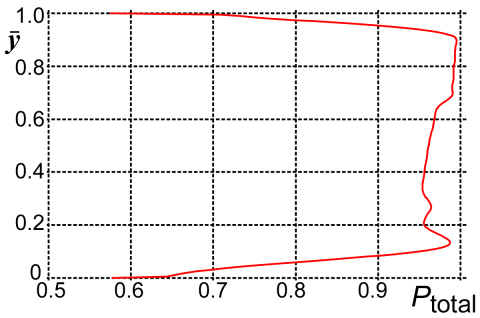

Figure 8. $P_{\rm total}$ in the exit section of the flow depicted in Fig. 6 versus the distance $\bar{y}$ from the bottom wall.

In the same way we calculated a dependence $x_{\rm sh}$ on M_∞ at a smaller pressure $p_{\rm exit} = 1.8\times10^5$ N/m^2, see curve 2 in Fig. 5. The reduction of $p_{\rm exit}$ yields a displacement of SW downstream to the exit. Therefore one needs smaller M_∞ to return SW to a position near the wall bend which admits its expulsion from the channel due to a small perturbation. That is why curve 2 in Fig. 5 is shifted to smaller M_∞ with respect to curve 1.

Figures 7, 8 illustrate the total pressure distribution in the flow depicted in Fig. 6. As seen, the total pressure losses in this regime noticeably differ from the ones displayed in Figs. 3, 4.

5. Shock wave location as a function of the angle of attack α.

Curve 1 in Fig. 9 presents a dependence of $x_{\rm sh}$ on α for $M_\infty = 1.62$. Both the numerical solution and oblique shock relations show that at $\alpha = -7^\circ$ (see the left endpoint of curve 1) the Mach number behind the bow oblique shock is $M_{\rm bow} = 1.378$. This value coincides with $M_{\rm bow}$ in the conditions $M_\infty = 1.55$, $\alpha = -5^\circ$ which correspond to the left endpoint of curve 1 in Fig. 5. However, the SW locations are different in these two cases, as they depend not only on $M_{\rm bow}$ but also on a triple shock configuration formed in front of the top wall. A detachment of the triple shock from the wall is much smaller at $M_\infty = 1.62$, $\alpha = -7^\circ$ than at $M_\infty = 1.55$, $\alpha = -5^\circ$. This explains a displacement of the whole shock system downstream and, as a consequence, the larger ordinate of the left endpoint of curve 1 in Fig. 9 than in Fig. 5.

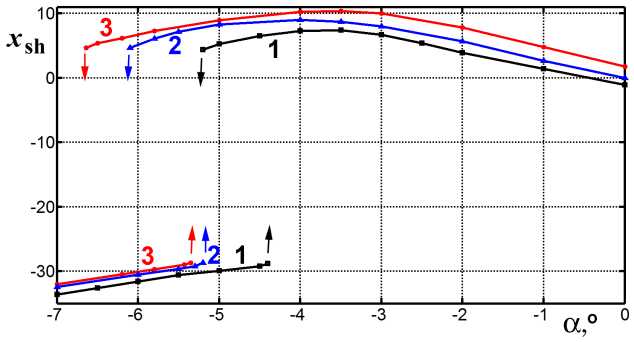

Figure 9. Coordinate $x_{\rm sh}$ of SW versus the angle of attack α: $1 - M_\infty = 1.62$, $p_\infty = 8\times10^4$, $p_{\rm exit} = 2\times10^5$; $2 - M_\infty = 1.63$, $p_\infty = 8\times10^4$, $p_{\rm exit} = 2\times10^5$; $3 - M_\infty = 1.63$, $p_\infty = 24\times10^4$, $p_{\rm exit} = 6\times10^5$.

With increasing α from -7° to -5° at $M_\infty = 1.62$, the Mach number $M_{\rm bow}$ behind the bow shock increases, and the detachment of triple shock from the top wall becomes small, see Fig. 2. Further increase of α to values larger than -4.4° triggers the swallowing of SW and transition from the lower branch of curve 1 in Fig. 9 to the upper one.

At a larger free-stream Mach number, $M_\infty = 1.63$, the Mach number $M_{\rm bow}$ decreases. Therefore, one needs smaller values of α to trigger the swallowing/expulsion of SW. That is why curve 2 in Fig. 9 is shifted to smaller M_∞ with respect to curve 1. Curve 3 presents results obtained for the tripled pressures p_∞ and $p_{\rm exit}$, which imply a tripled Reynolds number. As seen, the larger pressures and Reynolds number produce a noticeable expansion of the hysteresis.

6. Shock wave location as a function of the exit pressure $p_{\rm exit}$.

Computations of $x_{\rm sh}$ versus $p_{\rm exit}$ were performed in a similar way. As seen from Fig. 10, the shock position exhibits a hysteresis, which is insignificantly larger at $M_\infty = 1.60$ than at $M_\infty = 1.62$. We notice that pressures $p_{\rm exit} < 1.8\times10^5$ N/m^2 lead to formation of local supersonic velocities at the exit and, consequently, require a revision of the exit condition.

To study an effect of smoothing the bottom wall corner, we performed flow computations for a modified channel obtained by a local replacement of corner (1) with a circular arc of radius R in a short interval $x_1 \le x \le x_2$; the arc is tangential to corner (1) at $x = x_1 < 8$ and $x = x_2 > 8$. We examined four values of R : (a) 38.12, (b) 63.52, (c) 101.65, (d) 190.60. In the cases (a) and (b), computations showed only insignificant distinctions of the plots $x_{\rm sh}(p_{\rm exit})$

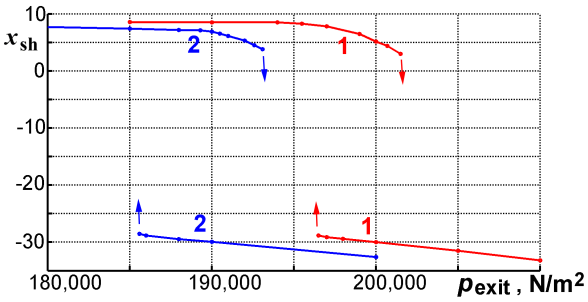

Figure 10. Coordinate $x_{\rm sh}$ of SW versus $p_{\rm exit}$ at $\alpha = -5°$: $1 - M_\infty = 1.62$, $2 - M_\infty = 1.60$.

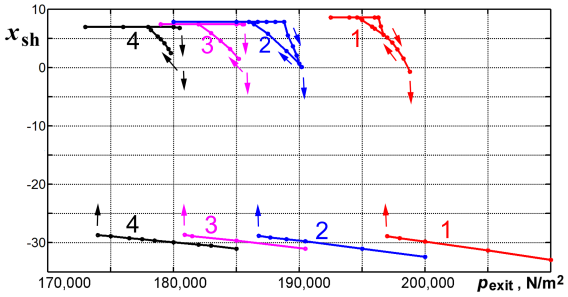

Figure 11. Coordinate $x_{\rm sh}$ of SW versus $p_{\rm exit}$ at $\alpha = -5°$ and radius $R = 190.6$ of the arc smoothing the bottom corner (1): $1 - M_\infty = 1.62$, $2 - M_\infty = 1.60$, $3 - M_\infty = 1.59$, $4 - M_\infty = 1.58$.

from those displayed in Fig. 10. Meanwhile, in the cases (c) and (d), computations revealed an extra hysteresis of SW location. In particular, Fig. 11 demonstrates a dependence of $x_{\rm sh}$ on $p_{\rm exit}$ obtained at $R = 190.60$. The extra hysteresis arises in the regime with a swallowed SW, see the upper branches of curves 1 - 4. It is attributed to the separated boundary layer like a flow hysteresis in straight nozzles [10]. The upper branches of curves 1 and 2 create loops, which illustrate steady positions of SW under step-by-step changes of $p_{\rm exit}$. Transitions from the most top branches of curves 3 and 4 to slightly lower branches (whose descent is about 45°) were performed through unsteady states as indicated by arrows.

7. Conclusions

Transonic flow in channels with a shift of the bottom wall corner downstream with respect to the top corner is studied numerically. The obtained solutions demonstrate non-unique flow regimes and significant hysteresis under gradual variations of the free-stream Mach number, angle of attack, or exit pressure. The Mach numbers under consideration are larger than those in [6] due to the smaller area of the exit. This enhances boundary layer separation from the lower wall and admits a double hysteresis when the bottom wall corner (1) is smoothed with a circular arc of sufficiently large radius.

Acknowledgments

This research was performed using computational resources provided by the Computational Center of St. Petersburg State University (http://cc.spbu.ru). The work was partially supported by the Russian Foundation for Basic Research under grant no. 19-01-00242.

References

[1] Torenbeek E and Wittenberg H 2009 *Flight Physics* (Dordrecht: Springer)
[2] Guo S, Wang Z and Zhao Y 2014 *J. National University of Defense Technology* **36** 10
[3] Kuzmin A 2016 *Archive Appl. Mech.* **86** 787
[4] Kotteda V M K and Mittal S 2016 *J. Propulsion and Power* **32** 171
[5] Feng S, Chang J, Zhang Ch, Wang Y, Ma J and Bao W 2017 *Aerospace Sci. and Technology* **67** 96
[6] Kuzmin A 2019 *Advances in Aircraft and Spacecraft Science* **6** 19
[7] Kuzmin A 2017 *Archive Appl. Mech.* **87** 1269
[8] Menter F R 2009 *Int. J. Comput. Fluid Dynamics* **23** 305
[9] Spalart P R and Allmaras S R 1994 *La Recherche Aérospatiale* no. 1, 5
[10] Setoguchi T, Matsuo S, Alam M M A, Nagao J and Kim H D 2010 *J Thermal Science* **19** 526